

# RIXS observation of bond-directional nearest-neighbor excitations in the Kitaev material $\text{Na}_2\text{IrO}_3$

M. Magnaterra,<sup>1</sup> K. Hopfer,<sup>1</sup> Ch. J. Sahle,<sup>2</sup> M. Moretti Sala,<sup>3</sup> G. Monaco,<sup>4</sup> J. Attig,<sup>5</sup> C. Hickey,<sup>5</sup> I.-M. Pietsch,<sup>6</sup> F. Breitner,<sup>6</sup> P. Gegenwart,<sup>6</sup> M. H. Upton,<sup>7</sup> Jungho Kim,<sup>7</sup> S. Trebst,<sup>5</sup> P. H. M. van Loosdrecht,<sup>1</sup> J. van den Brink,<sup>8,9</sup> and M. Grüninger<sup>1</sup>

<sup>1</sup>*Institute of Physics II, University of Cologne, 50937 Cologne, Germany*

<sup>2</sup>*ESRF, The European Synchrotron, 71 Avenue des Martyrs, CS40220, 38043 Grenoble Cedex 9, France*

<sup>3</sup>*Dipartimento di Fisica, Politecnico di Milano, I-20133 Milano, Italy*

<sup>4</sup>*Dipartimento di Fisica e Astronomia "Galileo Galilei", Università di Padova, Padova, Italy*

<sup>5</sup>*Institute for Theoretical Physics, University of Cologne, 50937 Cologne, Germany*

<sup>6</sup>*Experimental Physics VI, Center for Electronic Correlations and Magnetism, University of Augsburg, 86159 Augsburg, Germany*

<sup>7</sup>*Advanced Photon Source, Argonne National Laboratory, Argonne, Illinois 60439, USA*

<sup>8</sup>*Institute for Theoretical Solid State Physics, IFW Dresden, 01069 Dresden, Germany*

<sup>9</sup>*Institute for Theoretical Physics and Würzburg-Dresden Cluster of Excellence ct.qmat, Technische Universität Dresden, 01069 Dresden, Germany*

(Dated: January 19, 2023)

Spin-orbit coupling locks spin direction and spatial orientation and generates, in semi-classical magnets, a local spin easy-axis and associated ordering. Quantum spin-1/2's defy this fate: rather than spins becoming locally anisotropic, the spin-spin interactions do. Consequently interactions become dependent on the spatial orientation of bonds between spins, prime theoretical examples of which are Kitaev magnets. Bond-directional interactions imply the existence of bond-directional magnetic modes, predicted spin excitations that render crystallographically equivalent bonds magnetically inequivalent, which yet have remained elusive experimentally. Here we show that resonant inelastic x-ray scattering allows us to explicitly probe the bond-directional character of magnetic excitations. To do so, we use a scattering plane spanned by one bond and the corresponding spin component and scan a range of momentum transfer that encompasses multiple Brillouin zones. Applying this approach to  $\text{Na}_2\text{IrO}_3$  we establish the different bond-directional characters of magnetic excitations at  $\sim 10$  meV and  $\sim 45$  meV. Combined with the observation of spin-spin correlations that are confined to a single bond, this experimentally validates the Kitaev character of exchange interactions long proposed for this material.

The physics of quantum magnets with bond-directional interactions can be captured by so-called compass models [1], quantum theories of matter in which the couplings between different spin components are inherently spatially (typically, direction) dependent. Theoretically, this class of models harbors a range of interesting emergent physical phenomena, including the frustration of (semi-)classical ordered states on unfrustrated lattices, and a boost of quantum effects, prompting, in certain cases, the appearance of quantum spin liquids [2–4] – Kitaev spin liquids are well-known examples [5, 6]. In spin-1/2 materials, spin-orbit coupling naturally induces bond-directional spin-spin interactions. These can dominate when spin-orbit coupling becomes large, e.g., in 4d and 5d transition metal compounds [7–9]. However it has remained a principal challenge to experimentally identify the fingerprints of bond-directional magnetic interactions [10] and to establish methods to systematically explore their consequences for elementary magnetic properties.

Here we show that bond-directional *excitations* (BDE) – spin excitations that render crystallographically equivalent directions magnetically inequivalent – are a hallmark of bond-directional magnetic *interactions* and demonstrate how to use resonant inelastic x-ray scattering (RIXS) to directly probe these BDE. The challenge to resolving the bond-directional character of magnetic modes is that it requires simultaneous knowledge of both the spin operator creating the excitation and the direction of the bond involved. We introduce a RIXS geometry that yields the former via the polarization dependence and the latter by measuring across *multiple* Brillouin zones. Using this method on  $\text{Na}_2\text{IrO}_3$ , a Kitaev material ex-

hibiting a proximate spin liquid regime [11–13], we establish the different bond-directional characters of spin-conserving and spin-flip excitations at  $\sim 10$  meV and  $\sim 45$  meV, respectively.

Resolving BDE with RIXS on  $\text{Na}_2\text{IrO}_3$  is based on polarization selection rules but a polarization analysis of the scattered x-rays is not available at the commonly used Ir  $L$  edge. We have solved this problem by exploiting a *tilted* sample geometry which highlights polarization effects over the large range of  $\mathbf{q}$  space that can be covered with hard x-rays, see Fig. 1. Tilting the sample puts the spin-orbit entangled  $j^z$  component of the local pseudo-spin  $j = 1/2$  moments into the scattering plane. This allows us to disentangle excitations of  $j^z$  from those of  $j^x$  or  $j^y$ . The anisotropy in  $j$  space translates into a characteristic  $\mathbf{q}$  dependence of the intensity that provides a direct signature of bond-directional behavior.

**Bond-directional character:** To illustrate the conceptual relation between bond-directional interactions and BDE we consider a central spin on site  $i$  surrounded by sites  $j$ , connected by bonds  $\gamma_{\langle ij \rangle}$  along crystallographically equivalent directions. When exchange interactions are bond-directional, the magnetic Hamiltonian  $H_\gamma$  for two spins on bond  $\gamma$  has the property that in general  $H_\gamma \neq H_{\gamma'}$  even if bonds  $\gamma$  and  $\gamma'$  are equivalent from a structural point of view. When one now creates a magnetic excitation by perturbing the central spin by operator  $\hat{O}_i$ , the commutator  $[H_{\gamma\langle ij \rangle}, \hat{O}_i]$  in general depends on  $\gamma$ . As a consequence this magnetic excitation distributes *unevenly* over the crystallographically equivalent bonds, breaking lattice symmetry.

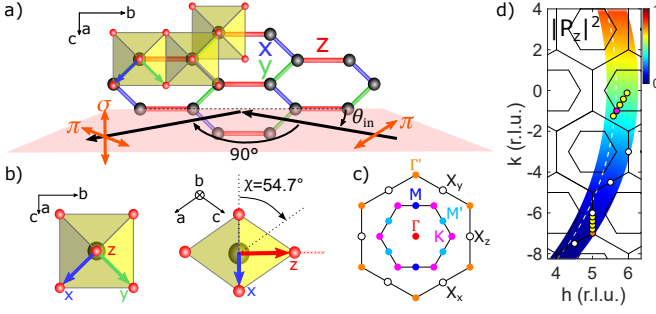


FIG. 1. (a) Sketch of scattering geometry with tilted sample. We use incident  $\pi$  polarization while the RIXS intensity is summed over outgoing  $\pi$  and  $\sigma$  polarizations. (b) Front and side views of a single  $\text{IrO}_6$  octahedron. For a tilt angle  $\chi = 54.7^\circ$ ,  $j^z$  lies in the scattering plane. (c) 2D high-symmetry points in the first and second Brillouin zones around  $\Gamma$ . A  $\Gamma$  point occurs for  $h + k$  even and  $k = 3m$  with integer  $m$  and  $h$ , see (d). BDE are most evident around  $X_\gamma$ . (d) Polarization factor  $|P^z(\mathbf{q})|^2$  across the covered  $\mathbf{q}$  range. The dashed line corresponds to scanning  $\theta_{\text{in}}$  from  $5^\circ$  to  $65^\circ$  for  $\chi = 54.7^\circ$  and scattering angle  $2\theta = 90^\circ$ . Experimentally, we vary  $\chi$  between  $52^\circ$  and  $64^\circ$ . Symbols mark the  $\mathbf{q}$  points addressed in Fig. 2. For the high-symmetry points, symbol colors refer to the sketch in c).

An elementary example in which BDE emerge is the honeycomb Kitaev model with  $H_\gamma = K S_i^\gamma S_j^\gamma$  where  $\gamma = x, y, z$  simultaneously denotes the three nearest-neighbor bonds and the three spin components, signifying the bond-directional character of the interaction. A local operator  $S_i^x$  commutes with  $H_x$  but not with  $H_y$  and  $H_z$  on the other two bonds, so that perturbing the system by  $S_i^x$  renders the three crystallographic bonds inequivalent and produces BDE. In particular  $S_i^x$  creates localized flux excitations on the two hexagons that share the  $x$  bond, while the third hexagon connected to site  $i$  remains unaffected, manifestly breaking the three-fold rotational symmetry of the flux distribution and consequently the Majorana modes scattered by the fluxes.

Single crystals of  $\text{Na}_2\text{IrO}_3$  were grown following the procedure described in [14] with 10 % extra Ir at 1323 K for 14 days. To establish the presence of BDE we measured RIXS at the Ir  $L_3$  edge at beamline ID20 at the ESRF [15, 16]. The incident energy  $E_{\text{in}} = 11.2145$  keV resonantly enhances magnetic excitations of the  $j = 1/2$  moments. The sample surface is parallel to the honeycomb plane, i.e., the  $ab$  plane. The  $b$  axis contains the  $z$  bond and lies in the horizontal scattering plane such that the incident beam is parallel to  $b$  for a vanishing angle of incidence  $\theta_{\text{in}}$ , see Fig. 1. With a tilt of the sample of  $\chi = 54.7^\circ$  around  $b$ , where  $\chi$  is the angle between the vertical and the honeycomb  $ab$  plane,  $j^z$  is lying in the scattering plane. The elastic contribution due to Thomson scattering is almost fully suppressed by strictly using a scattering angle  $2\theta = 90^\circ$ , where all outgoing polarization contributions are perpendicular to the incident  $\pi$  polarization. The resolution  $\delta\mathbf{q}$  of the transferred momentum equals about  $(\pm 0.05 \pm 0.1 \pm 0.05)$  reciprocal lattice units (r.l.u.) using a 60 mm iris on the  $R = 2$  m Si(844) spherical diced analyzer. The energy resolution is  $\delta E = 25$  meV. All RIXS data were corrected for self-absorption [17].

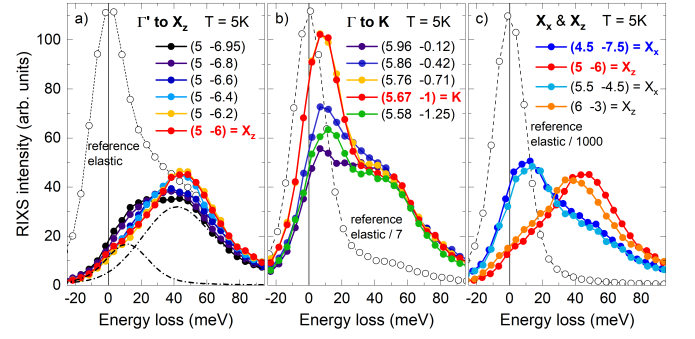


FIG. 2. RIXS spectra at 5 K at selected  $\mathbf{q}$  points. (a)  $\Gamma'$  to  $X_z$ , (b)  $\Gamma$  to  $K$ , (c)  $X_x$  and  $X_z$ , cf. Fig. 1. The spectra show two peaks at about 10 meV and 45 meV which we attribute to predominantly local nearest-neighbor excitations. Dash-dotted lines in (a) distinguish the two peaks at (5 -6.95). Reference spectra recorded with  $2\theta \neq 90^\circ$  and a corresponding large elastic line mark zero energy loss (open symbols, scaled down as indicated). In (c), the different intensities of the two peaks at  $X_x$  and  $X_z$  provide direct evidence of BDE.

RIXS spectra measured at 5 K at selected  $\mathbf{q}$  points show two inelastic features peaking around 10 meV and 45 meV, see Fig. 2. Their magnetic character is demonstrated by the resonance behavior measured at 30 K, i.e., above the 3D ordering temperature  $T_N = 15$  K, see *Supplementary Information* [18]. Our focus is on the bond-directional character of excitations expected for a Kitaev material, not on low-energy magnons of the ordered state. In previous RIXS studies, the broad continuum peaking around 45 meV has been established as a generic, quasi-2D magnetic excitation of the  $j = 1/2$  honeycomb iridates which persists up to 300 K [13, 19–21]. A similar continuum has been observed in the  $j = 1/2$  honeycomb compound  $\alpha\text{-RuCl}_3$  [22, 23]. The 10 meV peak is particularly pronounced at the  $K$  point, which agrees with first RIXS results collected with improved energy resolution  $\delta E = 12$  meV [19]. Observation of the 10 meV feature with  $\delta E = 25$  meV requires excellent suppression of elastic Thomson scattering which we achieve by using  $2\theta = 90^\circ$ . For comparison, reference spectra (open symbols) measured with  $2\theta \neq 90^\circ$  are peaking at zero energy loss.

In general, RIXS spectra as a function of energy loss are appropriate to study dispersive modes. However, for both inelastic features the peak energies hardly depend on  $\mathbf{q}$ , see Fig. 2. The key to a microscopic understanding of the two predominantly local excitations is the  $\mathbf{q}$ -dependent intensity  $I(\mathbf{q}, \omega)$ . This is most evident from the astounding behavior at  $X_x$  and  $X_z$ , see Fig. 2c). These  $\mathbf{q}$  points are fully equivalent for the honeycomb lattice but probe different bond directions in the case of nearest-neighbor excitations, as argued below. We will show that a small value of the polarization factor  $|P^z(\mathbf{q})|^2$  depicted in Fig. 1d) suppresses  $j^z$ -conserving excitations and enhances  $j^z$ -flip modes. This suppresses the spin-conserving 10 meV feature and enhances the 45 meV spin-flip mode at  $X_z$  but not at  $X_x$ , i.e., on  $z$  bonds but not on  $x$  bonds. Hence  $I(\mathbf{q}, \omega)$  demonstrates that the magnetic honeycomb lattice of  $\text{Na}_2\text{IrO}_3$  hosts BDE that have spin-flip or spin-conserving character.

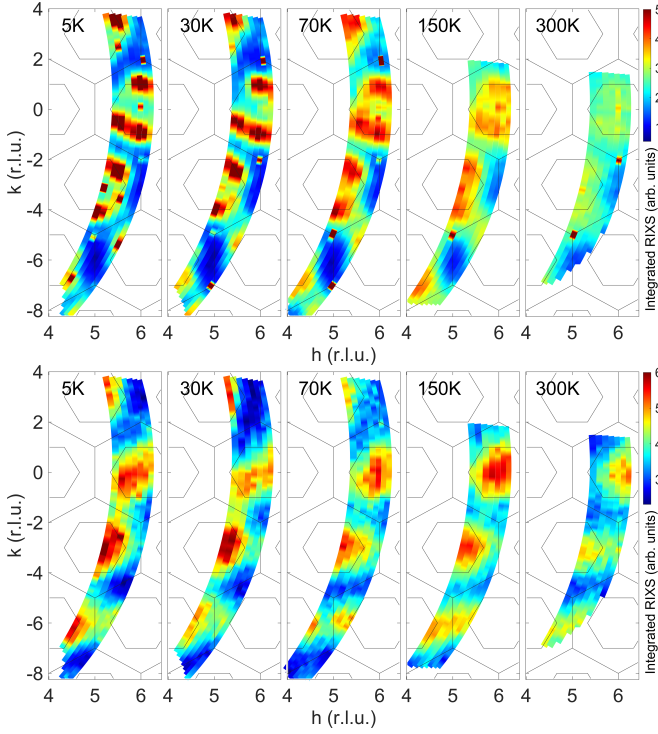


FIG. 3. **RIXS intensity maps at different temperatures**, integrated from -15 to 15 meV (top) and from 45 to 125 meV (bottom), focusing on the behavior of the two peaks shown in the spectra, cf. Fig. 2. At low energy, the narrow spots for integer  $h$  and  $k$  such as at (6 2) correspond to tails of structural Bragg peaks.

*RIXS intensity maps:* Figure 3 depicts 2D  $\mathbf{q}$ -space maps of  $I(\mathbf{q})$  integrated below 15 meV and above 45 meV, respectively. The integration ranges have been chosen to disentangle the different behavior of the two peaks observed in the spectra. For the continuum peaking around 45 meV, the quasi-2D character is supported by the gradual evolution with temperature  $T$ , see bottom panels in Fig. 3. This insensitivity to  $T$  and in particular to  $T_N$  agrees with previous RIXS results [13] for selected values of  $\mathbf{q}$ . The overall behavior with a broad peak centered at  $\Gamma$  can be described by nearest-neighbor correlations (see below).

To study the 10 meV peak, we have to cope with the fact that the dominant contribution to the low-energy intensity below  $T_N$  stems from elastic magnetic Bragg scattering with the 3D ordering wave vector  $\mathbf{Q}_0 = (0 \ 1 \ 1/2)$  [24, 25] and from low-energy magnons that are expected to emerge from there. In the 2D ( $h \ k$ ) maps, the magnetic Bragg spots are not hit perfectly since the value of  $l$  is adapted to achieve  $2\theta = 90^\circ$ . Nevertheless we find pronounced maxima at  $M = \Gamma \pm (0 \ 1)$  and enhanced intensity at  $M'$ , cf. Fig. 1c). The narrow features at  $M$  and  $M'$  are evident in Fig. 4a), which shows the same 5 K data as panel b) but on another color scale. Chun *et al.* [10] analyzed the elastic scattering at  $M$  and  $M'$  to derive the existence of dominant Kitaev exchange interactions in  $\text{Na}_2\text{IrO}_3$ . In contrast, we focus on the inelastic response not too close to  $M$  and  $M'$ .

With decreasing temperature, the low-energy maps in the

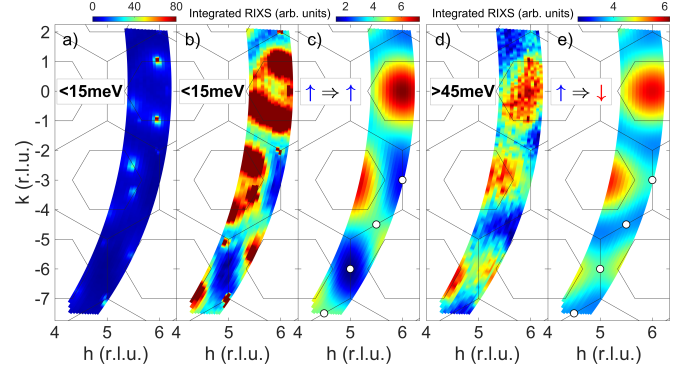


FIG. 4. **Maps of the RIXS intensity** at 5 K integrated from -15 to 15 meV ((a), (b)) and from 45 to 125 meV (d). Compared to Fig. 3, the data were measured on a finer mesh in  $\mathbf{q}$  space. Panels (a) and (b) show the same data on different color scales. The bond-directional character is apparent from polarization-related differences of the RIXS intensity at, e.g., the  $X_\gamma$  points (white circles). (c), (e): Predictions of a simple bond model for BDE with spin-conserving and spin-flip character, respectively, see Eqs. (1) and (2). Excitations are restricted to either an  $x$ ,  $y$ , or  $z$  bond with corresponding correlations of  $j^x$ ,  $j^y$ , or  $j^z$ , respectively. The calculated modulation pattern reflects nearest-neighbor correlations, cf. Fig. 5.

top panels of Fig. 3 show the building up of intensity close to  $M$ , reflecting the evolution of longer-range 3D correlations. However, central to our study is the behavior in  $\mathbf{q}$  ranges not too close to  $M$  such as around the four  $X_\gamma$  points marked by white symbols in Fig. 4b). There, also the low-energy maps are insensitive to  $T$ , and the data at 5 K and  $30 \text{ K} \approx 2T_N$  are very similar. In agreement with the spectra, cf. Fig. 2c), the low-energy maps show extended ranges of low intensity around  $X_z = (5 \ -6)$  and  $X_z = (6 \ -3)$  but larger intensity around  $X_x = (4.5 \ -7.5)$  and  $X_x = (5.5 \ -4.5)$ . The opposite behavior is observed for the 45 meV continuum in the high-energy maps, again in agreement with the spectra. The tilted sample geometry of our experiment has been designed to address this particular behavior via the polarization factors, revealing a clear signature of bond-directional behavior, as we will show below.

Below  $T_N$ , magnetic order breaks the three-fold rotational symmetry of the honeycomb lattice. However, immediately above  $T_N$  short-range zigzag correlations of all three domains were observed with equal strength [10]. Therefore, the inequivalence of  $X_x$  and  $X_z$  above  $T_N$  and the corresponding breaking of rotational symmetry cannot be attributed to long-range magnetic order. Furthermore, the RIXS intensity at  $X_\gamma$  is insensitive to  $l$ , and the intensity maps measured at 5 K on two different magnetic domains are very similar, see *Supplementary Information* [18]. All of these results firmly establish the quasi-2D character of the studied excitations.

*Nearest-neighbor correlations:* From the RIXS intensity maps we now establish the predominance of nearest-neighbor correlations, which will allow us to, e.g., identify the response at  $X_\gamma$  with the  $\gamma$  bond. A magnetically ordered state is characterized by long-range spin-spin correlations. Above the ordering temperature  $T_N$ , thermal fluctuations yield a strong decrease of the correlation length. In quasi-2D com-



pounds, short-range correlations typically survive at temperatures much higher than  $T_N$  [26]. The Kitaev model describes a very different case in which spin-spin correlations are strictly restricted to two nearest neighbors on a single bond.

This unusual scenario of nearest-neighbor correlations leaves clear fingerprints in the  $\mathbf{q}$  dependence of the RIXS intensity [13]. The dynamical structure factor of two sites has sinusoidal shape, i.e., the two-site scattering problem is equivalent to an inelastic incarnation of Young's double-slit experiment [27]. Summing over the three different bonds one finds

$$I_{\text{nn}}(\mathbf{q}) = I_0 + \sum_{\gamma} I_{\gamma}(\mathbf{q}) \cos^2(\mathbf{q} \cdot \Delta \mathbf{R}_{\gamma}/2), \quad (1)$$

where  $\Delta \mathbf{R}_{\gamma} = \mathbf{R}_2 - \mathbf{R}_1$  denotes a  $\gamma$  bond with two correlated nearest-neighbor Ir sites,  $I_0$  is a background intensity, and  $I_{\gamma}$  depends on the polarization. Such sinusoidal behavior has been observed for the continuum in the Kitaev material  $\alpha$ - $\text{RuCl}_3$  in inelastic neutron scattering [23]. In RIXS on the honeycomb iridates, Eq. (1) has been found to describe the integrated intensity of the continuum along  $\Gamma$ - $M$ - $\Gamma'$  and  $\Gamma$ - $K$ - $X$  [13], treating  $I_0$  and  $I_{\gamma}$  as empirical fit parameters. In Fig. 5, we visualize the sinusoidal intensity modulation of each bond for  $I_{\gamma} = 1$  and  $I_0 = 0$ . The sum  $I_{\text{nn}}(\mathbf{q})$  in the right panel yields broad maxima at  $\Gamma$  and reduced intensity at  $\Gamma'$ . Comparing  $I_{\text{nn}}(\mathbf{q})$  with the high-energy maps in the bottom panels of Fig. 3 demonstrates that already this simple picture of individual bonds describes the behavior of the continuum surprisingly well. For integration below 15 meV, the RIXS intensity in the first Brillouin zone is dominated, at low temperature, by longer-range correlations of zigzag type, as discussed above. For  $\mathbf{q}$  points not too close to  $M$  and  $M'$ , a convincing description in terms of the nearest-neighbor model requires considering the polarization-dependent matrix elements, as done in Fig. 4c) and discussed below.

In such a nearest-neighbor scenario with two-site structure factors  $F_{\gamma} = \cos^2(\mathbf{q} \cdot \Delta \mathbf{R}_{\gamma}/2)$ , the data at  $X_{\gamma}$  selectively probe the response of the  $\gamma$  bond. For instance  $X_z = (5 \text{ } -6)$  hosts a maximum of  $F_z$  with vanishing contributions from  $x$  and  $y$  bonds, see Fig. 5, while  $X_x = (4.5 \text{ } -7.5)$  shows a maximum of  $F_x$  with  $F_y = F_z = 0$ .

**Bond-directional excitations:** With this information on the bond direction, we utilize polarization selection rules to address bond-directional behavior, i.e., whether the application of, e.g., the local operator  $S_i^x$  creates an excitation connected to a specific bond. In the Kitaev model, a RIXS excitation on the  $\gamma$  bond requires to apply  $P^{\gamma} S_i^{\gamma}$  [28, 29] with the polarization factor  $\mathbf{P} = i\boldsymbol{\varepsilon}' \times \boldsymbol{\varepsilon}$  and the incident and outgoing polarizations  $\boldsymbol{\varepsilon}$  and  $\boldsymbol{\varepsilon}'$ , respectively. As shown below, this describes the behavior of the 10 meV feature but disagrees with the different polarization properties of the 45 meV continuum. Therefore, we employ a complementary microscopic approach and start from the RIXS matrix element for magnetic excitations of a  $j = 1/2$  moment at site  $\mathbf{R}_i$  [30]. With the outgoing  $\pi$  and  $\sigma$  polarizations being perpendicular to the incident polarization, see Fig. 1, this matrix element is proportional to  $\mathbf{P} \cdot \mathbf{S}_i$ , where  $\mathbf{S}_i$  operates within the  $j = 1/2$  subspace. For the two sites of, e.g., a  $z$  bond, we consider that  $S_i^z$  creates a spin-conserving (sc) excitation while  $S_i^x$  or  $S_i^y$  yield a spin flip (sf) of the  $z$

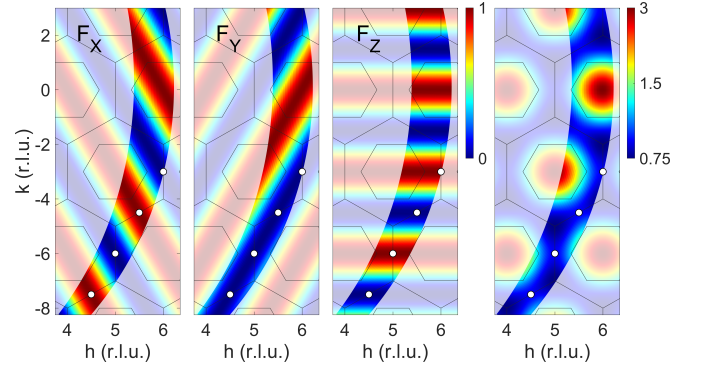


FIG. 5. **Sinusoidal two-site modulation patterns.** The three panels on the left depict the structure factor  $F_{\gamma} = \cos^2(\mathbf{q} \cdot \Delta \mathbf{R}_{\gamma}/2)$  for individual  $\gamma$  bonds with  $\gamma = x, y, z$ , see Eq. (1). The measured  $\mathbf{q}$  range is highlighted, cf. Fig. 3. Right: Sum over  $x, y$ , and  $z$  bonds. White circles mark  $X_x$  and  $X_z$  points, these are relevant for the discussion of the bond-directional character, see Fig. 2c).

component. For  $I_{\gamma}(\mathbf{q})$  in Eq. (1) this yields

$$I_z^{\text{sc}}(\mathbf{q}) \propto |P^z(\mathbf{q})|^2 \text{ and } I_z^{\text{sf}}(\mathbf{q}) \propto |P^x(\mathbf{q})|^2 + |P^y(\mathbf{q})|^2 \quad (2)$$

and equivalent expressions for  $x$  and  $y$  bonds. We have chosen the experimental geometry with the aim to strongly suppress  $|P^z(\mathbf{q})|^2$  in the lower parts of the maps, see Fig. 1d). More precisely,  $|P^z|^2 \propto \sin^2(\theta_{\text{in}})$ , and the angle of incidence  $\theta_{\text{in}}$  is varied from about  $5^\circ$  to  $65^\circ$ . This corresponds to an  $(h \text{ } k)$  range where  $k$  roughly runs from  $-8$  to  $4$  and depends roughly linearly on  $\theta_{\text{in}}$ . In contrast,  $|P^x(\mathbf{q})|^2$  and  $|P^y(\mathbf{q})|^2$  are nearly constant and large, see *Supplementary Information* [18]. In the bond-directional scenario described by Eq. (2), the suppression of  $|P^z|^2$  switches off spin-conserving excitations on  $z$  bonds while it reduces the intensity of spin-flip excitations on  $x$  or  $y$  bonds by about a factor 2. This explains the stunning difference of the spectra measured at  $X_z$  and  $X_x$ , see Fig. 2c), if we attribute the peaks at 10 and 45 meV to spin-conserving and spin-flip excitations, respectively, and identify  $X_{\gamma}$  with the  $\gamma$  bond, as appropriate for nearest-neighbor correlations.

Finally, we calculate maps of the RIXS intensity  $I_{\text{nn}}(\mathbf{q})$  expected for BDE, see Eq. (1). This combines the sinusoidal structure factors  $F_{\gamma}$  of the nearest-neighbor model, containing information on the bond direction, with the polarization-dependent  $I_{\gamma}(\mathbf{q})$  given in Eq. (2), reflecting the involved spin component. Figures 4c) and 4e) plot  $I_{\text{nn}}(\mathbf{q})$  for spin-conserving and spin-flip excitations, respectively. The excellent agreement with the RIXS data in panels b) and d) corroborates the above assignment of spin-conserving and spin-flip excitations at low and high energies, respectively. The continuum, integrated above 45 meV, is described very well over the entire range of  $\mathbf{q}$  and for all studied temperatures. For integration below 15 meV, our nearest-neighbor model represents the RIXS data very well at high  $T$  such as 70 K or 150 K. At 5 K, it still captures the behavior not too close to  $M$ , while the response in the vicinity of  $M$  reflects longer-range correlations. Altogether, bond-directional behavior is most evident around  $X_{\gamma}$  points. For instance  $X_x$  and  $X_z$  are equivalent on the honeycomb lattice and within the nearest-neighbor model for



isotropic  $I_\gamma = 1$ , see Fig. 5. The anisotropic, bond-directional character of the magnetic excitations in  $\text{Na}_2\text{IrO}_3$  yields very different RIXS intensities around  $X_x$  and  $X_z$  as well as different behavior at low and high energy.

**Outlook:** In the quest to identify Kitaev materials, the observation of bond-directional excitations via our advanced RIXS scheme can play a decisive role in validating, for a given compound, the presence of bond-directional interactions. These are appreciated as a source of frustration beyond the geometric frustration of non-bipartite lattices and key to the emergence of non-conventional forms of magnetism (such as recently discussed for fcc  $j = 1/2$   $\text{Ba}_2\text{CeIrO}_6$  [31]) and potentially spin liquid ground states (as hypothesized [32] for  $j = 1/2$  pyrochlore  $\text{Yb}_2\text{Ti}_2\text{O}_7$ ). A first step in this direction might be to apply our approach to other honeycomb Kitaev materials, but also to  $j = 1/2$  systems which have not attracted primary interest for bond-directional exchanges such as  $\text{Sr}_2\text{IrO}_4$ . In further developing our experimental approach a natural next step is to validate other forms of bond-directional interactions, such as dominating off-diagonal  $\Gamma$ -interactions [8, 9], and their manifestation in bond-directional excitations.

## ACKNOWLEDGMENTS

We thank A. Revelli for experimental support and useful discussions. We gratefully acknowledge the European Synchrotron Radiation Facility (ESRF) and the Advanced Photon Source (APS) for providing beam time and technical support. Prior to the measurements at ESRF shown here, we had performed a proof-of-principles RIXS study at beamline 27-ID at APS for the feasibility of this measurement geometry with a large sample tilt angle  $\chi$ . APS is a U.S. Department of Energy (DOE) Office of Science user facility operated for the DOE Office of Science by Argonne National Laboratory under Contract No. DE-AC02-06CH11357. Furthermore, we acknowledge funding from the Deutsche Forschungsgemeinschaft (DFG, German Research Foundation) via Project numbers 277146847 (CRC 1238, projects B03, C03), 247310070 (CRC 1143, project A05), and 107745057 (TRR 80).

- 
- [1] Z. Nussinov and J. van den Brink, Compass models: Theory and physical motivations, *Rev. Mod. Phys.* **87**, 1 (2015).
  - [2] C. Broholm, R. J. Cava, S. A. Kivelson, D. G. Nocera, M. R. Norman, and T. Senthil, Quantum spin liquids, *Science* **367**, eaay0668 (2020).
  - [3] L. Savary and L. Balents, Quantum spin liquids: a review, *Reports on Progress in Physics* **80**, 016502 (2016).
  - [4] J. Knolle and R. Moessner, A Field Guide to Spin Liquids, *Annual Review of Condensed Matter Physics* **10**, 451 (2019).
  - [5] A. Kitaev, Anyons in an exactly solved model and beyond, *Annals of Physics* **321**, 2 (2006).
  - [6] M. Hermanns, I. Kimchi, and J. Knolle, Physics of the Kitaev Model: Fractionalization, Dynamic Correlations, and Material Connections, *Annual Review of Condensed Matter Physics* **9**, 17 (2018).
  - [7] G. Jackeli and G. Khaliullin, Mott Insulators in the Strong Spin-Orbit Coupling Limit: From Heisenberg to a Quantum Compass and Kitaev Models, *Phys. Rev. Lett.* **102**, 017205 (2009).
  - [8] J. G. Rau, E. K.-H. Lee, and H.-Y. Kee, Spin-Orbit Physics Giving Rise to Novel Phases in Correlated Systems: Iridates and Related Materials, *Annual Review of Condensed Matter Physics* **7**, 195 (2016).
  - [9] S. Trebst and C. Hickey, Kitaev materials, *Physics Reports* **950**, 1 (2022).
  - [10] S. H. Chun, J.-W. Kim, J. Kim, H. Zheng, C. C. Stoumpos, C. D. Malliakas, J. F. Mitchell, K. Mehlawat, Y. Singh, Y. Choi, T. Gog, A. Al-Zein, M. Moretti Sala, M. Krisch, J. Chaloupka, G. Jackeli, G. Khaliullin, and B. J. Kim, Direct evidence for dominant bond-directional interactions in a honeycomb lattice iridate  $\text{Na}_2\text{IrO}_3$ , *Nature Physics* **11**, 462 (2015).
  - [11] A. Banerjee, C. A. Bridges, J. Q. Yan, A. A. Aczel, L. Li, M. B. Stone, G. E. Granroth, M. D. Lumsden, Y. Yiu, J. Knolle, S. Bhattacharjee, D. L. Kovrizhin, R. Moessner, D. A. Tennant, D. G. Mandrus, and S. E. Nagler, Proximate Kitaev quantum spin liquid behaviour in a honeycomb magnet, *Nature Materials* **15**, 733 (2016).
  - [12] K. Mehlawat, A. Thamizhavel, and Y. Singh, Heat capacity evidence for proximity to the Kitaev quantum spin liquid in  $\text{A}_2\text{IrO}_3$  ( $\text{A} = \text{Na}, \text{Li}$ ), *Phys. Rev. B* **95**, 144406 (2017).
  - [13] A. Revelli, M. Moretti Sala, G. Monaco, C. Hickey, P. Becker, F. Freund, A. Jesche, P. Gegenwart, T. Eschmann, F. L. Buessen, S. Trebst, P. H. M. van Loosdrecht, J. van den Brink, and M. Grüninger, Fingerprints of Kitaev physics in the magnetic excitations of honeycomb iridates, *Phys. Rev. Research* **2**, 043094 (2020).
  - [14] Y. Singh and P. Gegenwart, Antiferromagnetic Mott insulating state in single crystals of the honeycomb lattice material  $\text{Na}_2\text{IrO}_3$ , *Phys. Rev. B* **82**, 064412 (2010).
  - [15] M. Moretti Sala, C. Henriquet, L. Simonelli, R. Verbeni, and G. Monaco, High energy-resolution set-up for Ir  $L_3$  edge RIXS experiments, *Journal of Electron Spectroscopy and Related Phenomena* **188**, 150 (2013).
  - [16] M. Moretti Sala, K. Martel, C. Henriquet, A. Al Zein, L. Simonelli, C. J. Sahle, H. Gonzalez, M.-C. Lagier, C. Ponchut, S. Huotari, R. Verbeni, M. Krisch, and G. Monaco, A high-energy-resolution resonant inelastic X-ray scattering spectrometer at ID20 of the European Synchrotron Radiation Facility, *Journal of Synchrotron Radiation* **25**, 580 (2018).
  - [17] M. Minola, G. Della, H. Gretarsson, Y. Y. Peng, Y. Lu, J. Porras, T. Loew, F. Yakhov, N. B. Brookes, Y. B. Huang, J. Pelli-ciari, T. Schmitt, G. Ghiringhelli, B. Keimer, L. Braicovich, and M. Le Tacon, Collective nature of spin excitations in superconducting cuprates probed by resonant inelastic x-ray scattering, *Phys. Rev. Lett.* **114**, 217003 (2015).
  - [18] The *Supplementary Information* discusses the resonance behavior, the insensitivity to  $l$  and to magnetic domains, and the full polarization factors.
  - [19] J. Kim, J. Chaloupka, Y. Singh, J. W. Kim, B. J. Kim, D. Casa, A. Said, X. Huang, and T. Gog, Dynamic Spin Correlations in the Honeycomb Lattice  $\text{Na}_2\text{IrO}_3$  Measured by Resonant Inelastic x-Ray Scattering, *Phys. Rev. X* **10**, 021034 (2020).
  - [20] S. H. Chun, P. P. Stavropoulos, H.-Y. Kee, M. Moretti Sala, J. Kim, J.-W. Kim, B. J. Kim, J. F. Mitchell, and Y.-J. Kim, Optical magnons with dominant bond-directional exchange inter-

- actions in the honeycomb lattice iridate  $\alpha$ -Li<sub>2</sub>IrO<sub>3</sub>, *Phys. Rev. B* **103**, L020410 (2021).
- [21] J. Kim, H. Zhao, and G. Cao, Resolution of zigzag magnetic correlations in Na-deficient Na<sub>x</sub>IrO<sub>3</sub> without long-range ordering, *Phys. Rev. B* **106**, 075157 (2022).
- [22] H. Suzuki, H. Liu, J. Bertinshaw, K. Ueda, H. Kim, S. Laha, D. Weber, Z. Yang, L. Wang, H. Takahashi, K. Fürsich, M. Minola, B. V. Lotsch, B. J. Kim, H. Yavaş, M. Daghofer, J. Chaloupka, G. Khaliullin, H. Gretarsson, and B. Keimer, Proximate ferromagnetic state in the Kitaev model material  $\alpha$  - RuCl<sub>3</sub>, *Nature Communications* **12**, 4512 (2021).
- [23] A. Banerjee, J. Yan, J. Knolle, C. A. Bridges, M. B. Stone, M. D. Lumsden, D. G. Mandrus, D. A. Tennant, R. Moessner, and S. E. Nagler, Neutron scattering in the proximate quantum spin liquid  $\alpha$  - RuCl<sub>3</sub>, *Science* **356**, 1055 (2017).
- [24] F. Ye, S. Chi, H. Cao, B. C. Chakoumakos, J. A. Fernandez-Baca, R. Custelcean, T. F. Qi, O. B. Korneta, and G. Cao, Direct evidence of a zigzag spin-chain structure in the honeycomb lattice: A neutron and x-ray diffraction investigation of single-crystal Na<sub>2</sub>IrO<sub>3</sub>, *Phys. Rev. B* **85**, 180403(R) (2012).
- [25] S. K. Choi, R. Coldea, A. N. Kolmogorov, T. Lancaster, I. I. Mazin, S. J. Blundell, P. G. Radaelli, Y. Singh, P. Gegenwart, K. R. Choi, S.-W. Cheong, P. J. Baker, C. Stock, and J. Taylor, Spin Waves and Revised Crystal Structure of Honeycomb Iridate Na<sub>2</sub>IrO<sub>3</sub>, *Phys. Rev. Lett.* **108**, 127204 (2012).
- [26] H. M. Rønnow, D. F. McMorrow, and A. Harrison, High-Temperature Magnetic Correlations in the 2D  $S = 1/2$  Antiferromagnet Copper Formate Tetradeuterate, *Phys. Rev. Lett.* **82**, 3152 (1999).
- [27] A. Revelli, M. M. Sala, G. Monaco, P. Becker, L. Bohatý, M. Hermanns, T. C. Koethe, T. Fröhlich, P. Warzanowski, T. Lorenz, S. V. Streltsov, P. H. M. van Loosdrecht, D. I. Khomskii, J. van den Brink, and M. Grüninger, Resonant inelastic x-ray incarnation of Young's double-slit experiment, *Science Advances* **5**, eaav4020 (2019).
- [28] G. B. Halász, N. B. Perkins, and J. van den Brink, Resonant Inelastic X-Ray Scattering Response of the Kitaev Honeycomb Model, *Phys. Rev. Lett.* **117**, 127203 (2016).
- [29] Reference [28] distinguishes spin-conserving and non-spin-conserving channels, referring to the spin of an electron in the RIXS process. We measure the non-spin-conserving channel in direct RIXS, which in terms of the local  $j = 1/2$  moments contains both  $j^\gamma$ -flip and  $j^\gamma$ -conserving excitations.
- [30] L. J. P. Ament, G. Khaliullin, and J. van den Brink, Theory of resonant inelastic x-ray scattering in iridium oxide compounds: Probing spin-orbit-entangled ground states and excitations, *Phys. Rev. B* **84**, 020403(R) (2011).
- [31] A. Revelli, C. C. Loo, D. Kiese, P. Becker, T. Fröhlich, T. Lorenz, M. Moretti Sala, G. Monaco, F. L. Buessen, J. Attig, M. Hermanns, S. V. Streltsov, D. I. Khomskii, J. van den Brink, M. Braden, P. H. M. van Loosdrecht, S. Trebst, A. Paramakanti, and M. Grüninger, Spin-orbit entangled  $j = \frac{1}{2}$  moments in Ba<sub>2</sub>CeIrO<sub>6</sub>: A frustrated fcc quantum magnet, *Phys. Rev. B* **100**, 085139 (2019).
- [32] J. D. Thompson, P. A. McClarty, D. Prabhakaran, I. Cabrera, T. Guidi, and R. Coldea, Quasiparticle Breakdown and Spin Hamiltonian of the Frustrated Quantum Pyrochlore Yb<sub>2</sub>Ti<sub>2</sub>O<sub>7</sub> in a Magnetic Field, *Phys. Rev. Lett.* **119**, 057203 (2017).

## Supplementary Information

### RIXS observation of bond-directional nearest-neighbor excitations in the Kitaev material $\text{Na}_2\text{IrO}_3$

M. Magnaterra,<sup>1</sup> K. Hopfer,<sup>1</sup> Ch. J. Sahle,<sup>2</sup> M. Moretti Sala,<sup>3</sup> G. Monaco,<sup>4</sup> J. Attig,<sup>5</sup> C. Hickey,<sup>5</sup> I.-M. Pietsch,<sup>6</sup> F. Breitner,<sup>6</sup> P. Gegenwart,<sup>6</sup> M. H. Upton,<sup>7</sup> Jungho Kim,<sup>7</sup> S. Trebst,<sup>5</sup> P. H. M. van Loosdrecht,<sup>1</sup> J. van den Brink,<sup>8,9</sup> and M. Grüninger<sup>1</sup>

<sup>1</sup>*Institute of Physics II, University of Cologne, 50937 Cologne, Germany*

<sup>2</sup>*ESRF, The European Synchrotron, 71 Avenue des Martyrs, CS40220, 38043 Grenoble Cedex 9, France*

<sup>3</sup>*Dipartimento di Fisica, Politecnico di Milano, I-20133 Milano, Italy*

<sup>4</sup>*Dipartimento di Fisica e Astronomia "Galileo Galilei", Università di Padova, Padova, Italy*

<sup>5</sup>*Institute for Theoretical Physics, University of Cologne, 50937 Cologne, Germany*

<sup>6</sup>*Experimental Physics VI, Center for Electronic Correlations and Magnetism, University of Augsburg, 86159 Augsburg, Germany*

<sup>7</sup>*Advanced Photon Source, Argonne National Laboratory, Argonne, Illinois 60439, USA*

<sup>8</sup>*Institute for Theoretical Solid State Physics, IFW Dresden, 01069 Dresden, Germany*

<sup>9</sup>*Institute for Theoretical Physics and Würzburg-Dresden Cluster of Excellence ct.qmat, Technische Universität Dresden, 01069 Dresden, Germany*

(Dated: January 19, 2023)

#### I. RESONANCE BEHAVIOR

The resonance behavior at the Ir  $L_3$  edge provides an unambiguous proof of the magnetic nature of the excitations at about 10 meV and 45 meV. For  $\text{Ir}^{4+}$  ions, magnetic excitations within the  $j = 1/2$  subspace are resonantly enhanced in a direct RIXS process that involves the promotion of a  $2p$  core electron to the  $t_{2g}$  orbitals [1]. For  $\text{Na}_2\text{IrO}_3$ , this  $t_{2g}$  resonance occurs for an incident energy  $E_{\text{in}} = 11.2145$  keV [2]. For comparison, the RIXS intensity of excitations to  $e_g$  orbitals in the iridates is maximized by choosing a 3 to 4 eV larger value of  $E_{\text{in}}$  [3]. We observe pronounced  $t_{2g}$  resonance behavior both around 10 meV and around 45 meV, see Fig. 1. The right panel shows a resonance map measured at (5 -5.9 -5) where the 45 meV continuum is pronounced while the 10 meV peak is suppressed, as demonstrated by the RIXS spectra in Fig. 2c) of the main text. In contrast, the data in the left panel of Fig. 1 were measured at (4.5 -7.1 -4.7) and show a dominant contribution of the 10 meV feature. The common  $t_{2g}$  resonance

behavior firmly corroborates the magnetic character of both excitations.

In contrast, the excitation of phonons corresponds to an *indirect* RIXS process that is boosted if  $e_g$  orbitals are involved [4]. However, phonons have not been detected in  $L_3$  edge RIXS data of Mott-insulating  $5d^5$  iridates with  $\text{Ir}^{4+}$  ions, see, e.g., Refs. [2, 3, 5–11]. The suppression of the phonon contribution can be explained by the well-screened and short-lived intermediate state  $\text{Ir } 2p^5 t_{2g}^6$  at the  $L_3$  edge. This has to be distinguished from the case of RIXS at the O  $K$  edge with  $E_{\text{in}} \approx 0.53$  keV, where the observation of phonon features in  $\alpha\text{-Li}_2\text{IrO}_3$  [12] can be attributed to the very different, long-lived intermediate state.

#### II. 2D CHARACTER OF EXCITATIONS AND INSENSITIVITY TO MAGNETIC DOMAINS

##### A. $l$ dependence

Below the Néel temperature  $T_N = 15$  K,  $\text{Na}_2\text{IrO}_3$  hosts long-range magnetic order with the 3D propagation vector  $\mathbf{Q}_0 = (0 \ 1 \ 1/2)$  [13, 14]. In the 3D ordered state, low-energy magnons are expected to emerge from  $\mathbf{Q}_0$  and to show a dispersion as a function of the transferred momentum  $\mathbf{q}$ . However, we focus on the magnetic excitations at about 10 meV and 45 meV that cannot be described as magnons of the long-range ordered phase. These features persist to temperatures far above  $T_N$ , see Fig. 3 of the main text, which provides strong evidence for a predominantly 2D character. Our study highlights the RIXS intensity of these 2D excitations in  $(h \ k)$  space not too close to  $M = (0 \pm 1)$  and  $M' = (\pm 1/2 \pm 1/2)$ , cf. Fig. 1c) in the main text. In the  $(h \ k)$  range relevant to us, the RIXS intensity is insensitive to  $l$  even at 5 K, which is demonstrated in Fig. 2, using  $X_z = (5 \ -6)$ ,  $X_x = (5.5 \ -4.5)$ , and  $K = (5.66 \ -3)$  as examples. Panels a) and b) show data as a function of  $l$  for integration of the RIXS intensity below 15 meV and above 45 meV. In the latter case, the RIXS intensity is roughly constant as a function of  $l$ . In particular, the intensity of the 45 meV feature is significantly lower at

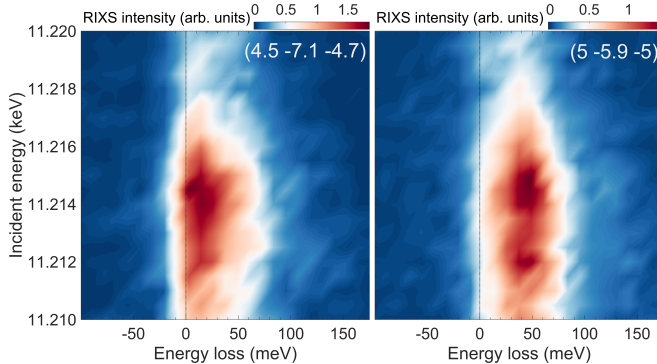


FIG. 1. **Resonance maps** of the magnetic excitations at 30 K. The 10 meV peak dominates for transferred momentum (4.5 -7.1 -4.7) (left), while the 45 meV continuum prevails at (5 -5.9 -5) (right). Both features show  $t_{2g}$  resonance at  $E_{\text{in}} = 11.2145$  keV (vertical scale). There is no evidence for an  $e_g$  resonance at  $E_{\text{in}} = 11.218$  keV. The elastic line at zero loss (solid black line) is suppressed by using a scattering angle  $2\theta = 90^\circ$ .



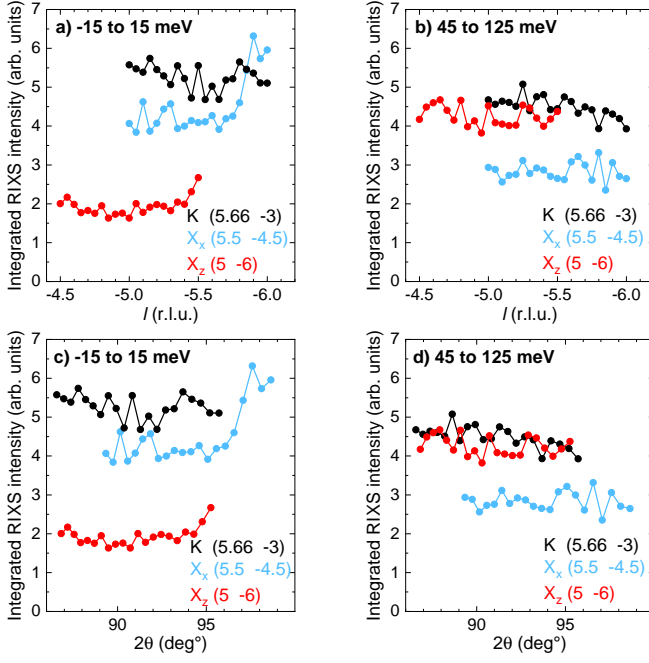


FIG. 2. **2D character of magnetic excitations.** Panels a) and b) depict the RIXS intensity at  $(5.66 -3 l)$ ,  $(5.5 -4.5 l)$ , and  $(5 -6 l)$  for integration below 15 meV and above 45 meV, respectively. The data have been collected at 5 K. Panels c) and d) show the same data plotted as a function of the scattering angle  $2\theta$ . At low energy, the contribution of the elastic line is suppressed for  $2\theta = 90^\circ$ .

$X_x$  than at  $X_z$  for all studied values of  $l$ . The 15 meV shows the opposite behavior, the RIXS intensity is higher at  $X_x$  than at  $X_z$ , again for all  $l$ . For integration from -15 to 15 meV, the contribution of the elastic line has to be considered. In the data shown in Figs. 2, 3, and 4 of the main text, the elastic line has been suppressed by choosing a scattering angle  $2\theta = 90^\circ$ . This, however, fixes  $l$  for a given  $(h k)$  point. Measuring the  $l$  dependence requires to change  $2\theta$  away from  $90^\circ$ . Therefore, we replot the same data in panels c) and d) as a function of  $2\theta$ . Close to  $90^\circ$ , the RIXS intensity is roughly constant also for integration below 15 meV, which strongly corroborates the 2D character. The increase of the low-energy intensity for  $2\theta$  further away from  $90^\circ$  arises from the increasing elastic contribution of Thomson scattering.

### B. 3D magnetic domains

The 2D character is further supported by the insensitivity of our results to 3D magnetic domains. The ideal 2D honeycomb lattice exhibits threefold rotational symmetry, such that the  $M$  points  $(0 \pm 1)$  and the  $M'$  points  $(\pm 1/2 \pm 1/2)$  all are equivalent. However, the 3D crystal structure of  $\text{Na}_2\text{IrO}_3$  shows a small monoclinic distortion, hence  $(0 \pm 1 1/2)$  and  $(\pm 1/2 \pm 1/2 1/2)$  are not equivalent. With the 3D propagation vector  $\mathbf{Q}_0 = (0 1 1/2)$  of long-range magnetic order [13, 14], the orientation of the zigzag ordering pattern is tied to the crystal structure.

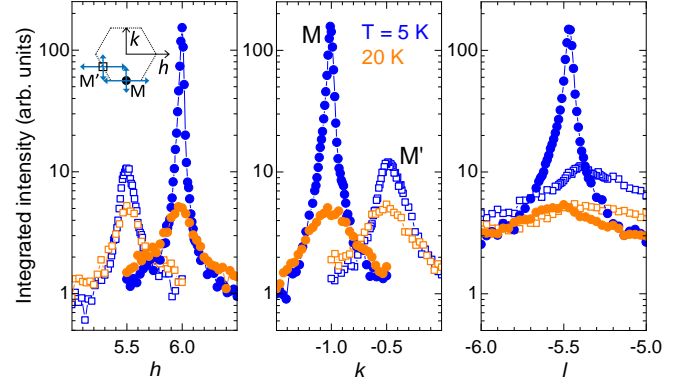


FIG. 3. **Quasielastic scans across a magnetic Bragg peak.** The scattered intensity was integrated from -15 meV to +15 meV. Full and open symbols show data across  $(6 -1 -5.5)$  and  $(5.5 -0.5 -5.5)$ , respectively. At 20 K, above  $T_N$ , both  $\mathbf{q}$  points show the same intensity. At 5 K,  $(6 -1 -5.5)$  hosts a magnetic Bragg peak.

Laue diffraction of our samples indicates structural  $120^\circ$  twinning in the honeycomb plane. The structural twins dictate the formation of corresponding magnetic domains. The cross section of the incident x-ray beam of roughly  $(15 \times 15) \mu\text{m}^2$  allows us to select the measurement spot such that a given twin domain dominates the response, as demonstrated by scans across  $M_{3D} = (6 -1 -5.5)$  and  $M'_{3D} = (5.5 -0.5 -5.5)$  for zero energy loss, see Fig. 3. At 20 K, i.e., above  $T_N$ , we observe clear peaks of the elastically scattered intensity along  $h$  and  $k$  but a broad intensity distribution along  $l$ . Furthermore, the intensity is very similar at  $M_{3D}$  and  $M'_{3D}$ . This suggests the coexistence of short-range 2D zigzag fragments running along three equivalent directions, in agreement with the results of Chun *et al.* [15]. At 5 K, we find a magnetic Bragg peak at  $M_{3D}$  that is characterized by a pronounced peak as a function of  $l$ . In contrast, the intensity at  $M'_{3D}$  is much lower and the peak still is very broad as a function of  $l$ . This demonstrates that the measurement predominantly probes a single magnetic domain.

In Fig. 4 we compare  $(h k)$  maps of the RIXS intensity measured at 5 K on two different spots of the sample that correspond to two different twin domains rotated by  $120^\circ$ . For each spot, we study the intensity integrated from -15 to 15 meV and from 45 to 125 meV. The intensity maps for the two different domains are very similar. In particular, the distinct behavior at different  $X_\gamma$  points is observed equivalently. This result corroborates that the different intensities at  $X_x$  and  $X_z$  cannot be attributed to small differences arising from the 3D crystal structure but reflect bond-directional excitations that are detected based on the polarization dependence. Note that the unambiguous determination of the character of a specific domain requires to address specific  $(h k l)$  points, the domain character cannot be read from  $(h k)$  maps measured with  $2\theta = 90^\circ$ .

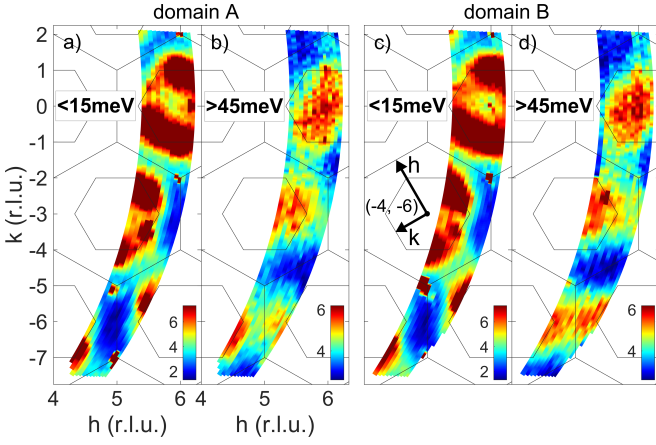


FIG. 4. **Maps of the RIXS intensity of two twin domains** measured at 5 K. Domain B is rotated by  $120^\circ$  with respect to domain A, as indicated by the coordinate frame in panel c). The intensity has been integrated from -15 to 15 meV and from 45 to 125 meV. The data agree on the bond-directional character of the magnetic excitations.

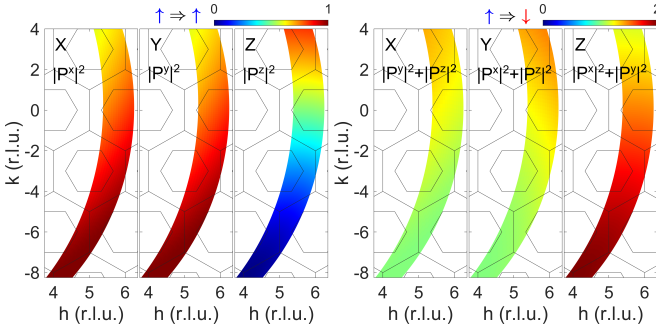


FIG. 5. **Polarization factors** of the three bonds. Left:  $|P^\gamma(\mathbf{q})|^2$ , applicable to spin-conserving excitations on a  $\gamma$  bond, as observed at 10 meV, cf. Eq. (5). The central feature is the suppression of  $|P^z(\mathbf{q})|^2$  in the lower part of the map, while  $|P^x|^2$  and  $|P^y|^2$  do not vary strongly with  $\mathbf{q}$ . Right: The panel for the  $z$  bond depicts  $|P^x(\mathbf{q})|^2 + |P^y(\mathbf{q})|^2$ , which is applicable to spin-flip excitations on the  $z$  bond, cf. Eq. (7). The other panels show equivalent expressions for  $x$  and  $y$  bonds. This describes the behavior of the 45 meV feature.

### III. POLARIZATION FACTORS

At the Ir  $L$  edge, the RIXS intensity  $I(\mathbf{q}, \omega)$  for excitations from the ground state  $|0\rangle$  to a final state  $|f\rangle$  is given by a coherent sum of scattering processes localized on individual sites. The sum is running over all sites  $\mathbf{R}_i$  at which a given final state  $|f\rangle$  can be reached, i.e., over which  $|f\rangle$  is delocalized. In dipole approximation one finds [1]

$$I(\mathbf{q}, \omega) = \sum_f \left| \langle f | \sum_i e^{i\mathbf{q} \cdot \mathbf{R}_i} [D^\dagger D]_{\mathbf{R}_i} | 0 \rangle \right|^2 \delta(\hbar\omega - E_f) \quad (1)$$

where  $E_f$  denotes the excitation energy and  $D$  is the local dipole operator. In general, magnetic excitations can be generated via different polarization channels [16]. We use  $2\theta = 90^\circ$  for the scattering angle, hence the outgoing vertical and horizontal polarizations  $\varepsilon'_\sigma$  and  $\varepsilon'_\pi$  are perpendicular to the linear incident polarization  $\varepsilon$ . In this case, the single-site RIXS matrix elements for magnetic excitations within the  $j = 1/2$  man-

ifold at site  $\mathbf{R}_i$  are given by [17]

$$[D^\dagger D]_{\mathbf{R}_i} = \frac{2}{3} \mathbf{P} \cdot \mathbf{S}_i \quad (2)$$

with the polarization factor  $\mathbf{P} = i\varepsilon' \times \varepsilon$ , and  $\mathbf{S}_i$  operates within the  $j = 1/2$  subspace. In the employed experimental geometry with  $2\theta = 90^\circ$ , see Fig. 1 of the main text, the polarization factor mainly depends on the angle of incidence  $\theta_{\text{in}}$ , which translates to a  $\mathbf{q}$  dependence of the polarization factor.

In terms of the diagonal components of the dynamical spin structure factor  $S(\mathbf{q}, \omega)$ ,

$$S^{\gamma\gamma}(\mathbf{q}, \omega) = \sum_f \left| \langle f | \sum_i e^{i\mathbf{q} \cdot \mathbf{R}_i} S_i^\gamma | 0 \rangle \right|^2 \delta(\hbar\omega - E_f), \quad (3)$$

the RIXS intensity can be written as

$$I(\mathbf{q}, \omega) \propto \sum_{\gamma \in \{x, y, z\}} |P^\gamma(\mathbf{q})|^2 S^{\gamma\gamma}(\mathbf{q}, \omega), \quad (4)$$

where, as usual, we neglect the off-diagonal components of  $S(\mathbf{q}, \omega)$ . In this form, the RIXS intensity thus measures the sum of the dynamical spin structure factor components weighted by their respective momentum-dependent polarization factors. We have chosen the experimental geometry such that  $|P^z(\mathbf{q})|^2$  strongly differs from the other components, see Fig. 5. By varying  $\mathbf{q}$ , one can thus vary the weighting of the different components of  $S(\mathbf{q}, \omega)$ , e.g. suppressing the contribution of  $S^{zz}(\mathbf{q}, \omega)$ .

Considering only nearest-neighbor correlations, the  $\mathbf{q}$  dependence of the dynamical structure factor is captured using only  $\cos^2(\mathbf{q} \cdot \Delta\mathbf{R}_{\gamma}/2)$  terms. For the 10 meV peak (spin-conserving excitations), the total intensity is well described by

$$I_{\text{nn}}^{\text{sc}}(\mathbf{q}) = \sum_{\gamma} |P^\gamma(\mathbf{q})|^2 \cos^2(\mathbf{q} \cdot \Delta\mathbf{R}_{\gamma}/2), \quad (5)$$

where the  $\mathbf{q}$  dependence of the structure factor is given by

$$S^{\gamma\gamma}(\mathbf{q}, 10 \text{ meV}) \propto \cos^2(\mathbf{q} \cdot \Delta\mathbf{R}_{\gamma}/2), \quad (6)$$

meaning that  $j^\gamma$  correlations dominate on  $\gamma$  bonds. For the 45 meV peak (spin-flip excitations), our data agree with

$$\begin{aligned} I_{\text{nn}}^{\text{sf}}(\mathbf{q}) &= \sum_{\gamma} \left[ \sum_{\gamma' \neq \gamma} |P^{\gamma'}(\mathbf{q})|^2 \right] \cos^2(\mathbf{q} \cdot \Delta\mathbf{R}_{\gamma}/2) \\ &= \sum_{\gamma} |P^\gamma(\mathbf{q})|^2 \left[ \sum_{\gamma' \neq \gamma} \cos^2(\mathbf{q} \cdot \Delta\mathbf{R}_{\gamma'}/2) \right], \end{aligned} \quad (7)$$

which yields

$$S^{\gamma\gamma}(\mathbf{q}, 45 \text{ meV}) \propto \sum_{\gamma' \neq \gamma} \cos^2(\mathbf{q} \cdot \Delta\mathbf{R}_{\gamma'}/2). \quad (8)$$

This means that, e.g., application of  $S_i^x$  creates a spin flip on either a  $y$  bond or a  $z$  bond. From Eqns. (5) and (7) one can read off  $I_{\gamma}^{\text{sc}}$  and  $I_{\gamma}^{\text{sf}}$  used in Eqns. (1) and (2) of the main text.

- 
- [1] L. J. P. Ament, M. van Veenendaal, T. P. Devereaux, J. P. Hill, and J. van den Brink, Resonant inelastic x-ray scattering studies of elementary excitations, *Rev. Mod. Phys.* **83**, 705 (2011).
- [2] A. Revelli, M. Moretti Sala, G. Monaco, C. Hickey, P. Becker, F. Freund, A. Jesche, P. Gegenwart, T. Eschmann, F. L. Buessen, S. Trebst, P. H. M. van Loosdrecht, J. van den Brink, and M. Grüninger, Fingerprints of Kitaev physics in the magnetic excitations of honeycomb iridates, *Phys. Rev. Research* **2**, 043094 (2020).
- [3] E. Lefrançois, A.-M. Pradipto, M. Moretti Sala, L. C. Chapon, V. Simonet, S. Picozzi, P. Lejay, S. Petit, and R. Ballou, Anisotropic interactions opposing magnetocrystalline anisotropy in  $\text{Sr}_3\text{NiIrO}_6$ , *Phys. Rev. B* **93**, 224401 (2016).
- [4] S. Moser, S. Fatale, P. Krüger, H. Berger, P. Bugnon, A. Magrez, H. Niwa, J. Miyawaki, Y. Harada, and M. Grioni, Electron-Phonon Coupling in the Bulk of Anatase  $\text{TiO}_2$  Measured by Resonant Inelastic X-Ray Spectroscopy, *Phys. Rev. Lett.* **115**, 096404 (2015).
- [5] J. Kim, M. Daghofer, A. H. Said, T. Gog, J. van den Brink, G. Khaliullin, and B. J. Kim, Excitonic quasiparticles in a spin-orbit Mott insulator, *Nature Communications* **5**, 4453 (2014).
- [6] M. Moretti Sala, V. Schnells, S. Boseggia, L. Simonelli, A. Al-Zein, J. G. Vale, L. Paolasini, E. C. Hunter, R. S. Perry, D. Prabhakaran, A. T. Boothroyd, M. Krisch, G. Monaco, H. M. Rønnow, D. F. McMorrow, and F. Mila, Evidence of quantum dimer excitations in  $\text{Sr}_3\text{Ir}_2\text{O}_7$ , *Phys. Rev. B* **92**, 024405 (2015).
- [7] X. Lu, D. E. McNally, M. Moretti Sala, J. Terzic, M. H. Upton, D. Casa, G. Ingold, G. Cao, and T. Schmitt, Doping Evolution of Magnetic Order and Magnetic Excitations in  $(\text{Sr}_{1-x}\text{La}_x)_3\text{Ir}_2\text{O}_7$ , *Phys. Rev. Lett.* **118**, 027202 (2017).
- [8] M. Rossi, M. Retegan, C. Giacobbe, R. Fumagalli, A. Efimenko, T. Kulka, K. Wohlfeld, A. I. Gubanov, and M. Moretti Sala, Possibility to realize spin-orbit-induced correlated physics in iridium fluorides, *Phys. Rev. B* **95**, 235161 (2017).
- [9] A. Revelli, C. C. Loo, D. Kiese, P. Becker, T. Fröhlich, T. Lorenz, M. Moretti Sala, G. Monaco, F. L. Buessen, J. Attig, M. Hermanns, S. V. Streltsov, D. I. Khomskii, J. van den Brink, M. Braden, P. H. M. van Loosdrecht, S. Trebst, A. Paramakanti, and M. Grüninger, Spin-orbit entangled  $j = \frac{1}{2}$  moments in  $\text{Ba}_2\text{CeIrO}_6$ : A frustrated fcc quantum magnet, *Phys. Rev. B* **100**, 085139 (2019).
- [10] J. Kim, J. Chaloupka, Y. Singh, J. W. Kim, B. J. Kim, D. Casa, A. Said, X. Huang, and T. Gog, Dynamic Spin Correlations in the Honeycomb Lattice  $\text{Na}_2\text{IrO}_3$  Measured by Resonant Inelastic x-Ray Scattering, *Phys. Rev. X* **10**, 021034 (2020).
- [11] S. H. Chun, P. P. Stavropoulos, H.-Y. Kee, M. Moretti Sala, J. Kim, J.-W. Kim, B. J. Kim, J. F. Mitchell, and Y.-J. Kim, Optical magnons with dominant bond-directional exchange interactions in the honeycomb lattice iridate  $\alpha\text{-Li}_2\text{IrO}_3$ , *Phys. Rev. B* **103**, L020410 (2021).
- [12] J. G. Vale, C. D. Dashwood, E. Paris, L. S. I. Veiga, M. Garcia-Fernandez, A. Nag, A. Walters, K.-J. Zhou, I.-M. Pietsch, A. Jesche, P. Gegenwart, R. Coldea, T. Schmitt, and D. F. McMorrow, High-resolution resonant inelastic x-ray scattering study of the electron-phonon coupling in honeycomb  $\alpha\text{-Li}_2\text{IrO}_3$ , *Phys. Rev. B* **100**, 224303 (2019).
- [13] F. Ye, S. Chi, H. Cao, B. C. Chakoumakos, J. A. Fernandez-Baca, R. Custelcean, T. F. Qi, O. B. Korneta, and G. Cao, Direct evidence of a zigzag spin-chain structure in the honeycomb lattice: A neutron and x-ray diffraction investigation of single-crystal  $\text{Na}_2\text{IrO}_3$ , *Phys. Rev. B* **85**, 180403(R) (2012).
- [14] S. K. Choi, R. Coldea, A. N. Kolmogorov, T. Lancaster, I. I. Mazin, S. J. Blundell, P. G. Radaelli, Y. Singh, P. Gegenwart, K. R. Choi, S.-W. Cheong, P. J. Baker, C. Stock, and J. Taylor, Spin Waves and Revised Crystal Structure of Honeycomb Iridate  $\text{Na}_2\text{IrO}_3$ , *Phys. Rev. Lett.* **108**, 127204 (2012).
- [15] S. H. Chun, J.-W. Kim, J. Kim, H. Zheng, C. C. Stoumpos, C. D. Malliakas, J. F. Mitchell, K. Mehlawat, Y. Singh, Y. Choi, T. Gog, A. Al-Zein, M. Moretti Sala, M. Krisch, J. Chaloupka, G. Jackeli, G. Khaliullin, and B. J. Kim, Direct evidence for dominant bond-directional interactions in a honeycomb lattice iridate  $\text{Na}_2\text{IrO}_3$ , *Nature Physics* **11**, 462 (2015).
- [16] M. W. Haverkort, Theory of Resonant Inelastic X-Ray Scattering by Collective Magnetic Excitations, *Phys. Rev. Lett.* **105**, 167404 (2010).
- [17] L. J. P. Ament, G. Khaliullin, and J. van den Brink, Theory of resonant inelastic x-ray scattering in iridium oxide compounds: Probing spin-orbit-entangled ground states and excitations, *Phys. Rev. B* **84**, 020403(R) (2011).